AGU PUBLICATIONS

JGR

Journal of Geophysical Research: Solid Earth

RESEARCH ARTICLE
10.1002/2017JB014804

Key Points:
- Wavefront tracking across USArray recovers amplification and attenuation maps for Rayleigh waves throughout the crust
- The use of ambient noise field allows for shorter period observations than previously available, at 8–32 s
- Comparisons to maps produced from earthquake-based observations at long periods confirm that the ambient noise field is suitable for these observations

Supporting Information:
- Supporting Information S1
- Data Set S1
- Data Set S2
- Data Set S3
- Data Set S4
- Data Set S5
- Data Set S6

Correspondence to:
D. C. Bowden,
dbowden@caltech.edu

Citation:
Bowden, D. C., Tsai, V. C., & Lin, F.-C. (2017). Amplification and attenuation across USArray using ambient noise wavefront tracking. *Journal of Geophysical Research: Solid Earth*, *122*. https://doi.org/10.1002/2017JB014804

Received 30 JUL 2017
Accepted 9 NOV 2017
Accepted article online 15 NOV 2017

Amplification and Attenuation Across USArray Using Ambient Noise Wavefront Tracking

Daniel C. Bowden[1], Victor C. Tsai[1], and Fan-Chi Lin[2]

[1]Seismological Laboratory, California Institute of Technology, Pasadena, CA, USA, [2]Department of Geology and Geophysics, University of Utah, Salt Lake City, UT, USA

Abstract As seismic traveltime tomography continues to be refined using data from the vast USArray data set, it is advantageous to also exploit the amplitude information carried by seismic waves. We use ambient noise cross correlation to make observations of surface wave amplification and attenuation at shorter periods (8–32 s) than can be observed with only traditional teleseismic earthquake sources. We show that the wavefront tracking approach can be successfully applied to ambient noise correlations, yielding results quite similar to those from earthquake observations at periods of overlap. This consistency indicates that the wavefront tracking approach is viable for use with ambient noise correlations, despite concerns of the inhomogeneous and unknown distribution of noise sources. The resulting amplification and attenuation maps correlate well with known tectonic and crustal structure; at the shortest periods, our amplification and attenuation maps correlate well with surface geology and known sedimentary basins, while our longest period amplitudes are controlled by crustal thickness and begin to probe upper mantle materials. These amplification and attenuation observations are sensitive to crustal materials in different ways than traveltime observations and may be used to better constrain temperature or density variations. We also value them as an independent means of describing the lateral variability of observed Rayleigh wave amplitudes without the need for 3-D tomographic inversions.

1. Introduction

Since the introduction of the Earthscope USArray, a network of more than 1,700 stations spanning the continental U.S., numerous studies have imaged seismic velocities in the crust and upper mantle (e.g., Ekström, 2014; Porritt et al., 2014; Shen et al., 2013). This has provided an unprecedented and cohesive view of tectonic structures within the continental U.S., ranging from broad patterns such as the transition from the recently tectonically active western U.S. to stable continental craton in the east, down to the description of smaller-scale provinces and features such as the Snake River Plain, Colorado Plateau, Reelfoot Rift, and others. The seismic models have been constructed (and are continuing to be constructed) through a range of seismic methods including surface wave tomography (one-station, two-station, and array-based methods; e.g., Jin & Gaherty, 2015; Liang & Langston, 2009), body-wave tomography (e.g., Schmandt & Lin, 2014), receiver functions (e.g., Kumar et al., 2012), and more, allowing for characterization of the shallowest crust down to the upper mantle.

While most of the above mentioned studies have focused on traveltimes and velocity modeling, there remains a wealth of information carried by the amplitudes of seismic data (e.g., Dalton & Ekström, 2006a; Ferreira & Woodhouse, 2007; Prieto et al., 2011; Weaver, 2011a). Notably, Lin, Tsai, and Ritzwoller (2012) and later Bao et al. (2016) successfully developed and applied a wavefront tracking method by which the effects of attenuation or amplification can be measured as Rayleigh waves from distant earthquakes propagate across the array. This approach considers how local geological structure can affect a passing wave's amplitudes in a manner both observable and different than what can be described purely by velocities. For example, material properties such as temperature or fluid content may be distinguishable using the complementary information of both seismic velocity and attenuation (e.g., Dalton & Ekström, 2006b; Karato, 1993; Priestley & McKenzie, 2006). Additionally, different seismic observables will be sensitive to geologic structure at different depths; the sensitivity kernels of Rayleigh wave amplification, horizontal-to-vertical (H/V) amplitude ratios, and group and phase velocity can all be used to probe different depths within the Earth (Lin, Schmandt, & Tsai, 2012; Lin, Tsai, & Ritzwoller, 2012; Lin et al., 2014).

The wavefront tracking approach used by Lin, Tsai, and Ritzwoller (2012) and Bao et al. (2016) extracts amplitude and phase traveltime observations of Rayleigh waves from distant earthquakes. Eddy and Ekström (2014)

used a somewhat different method based on amplitude differences between nearby stations to constrain amplifications, but this work also used earthquake data from USArray. In this paper, we use a wavefront tracking approach applied instead to ambient noise cross correlations. Ambient noise tomography has been increasingly used to recover velocity models, in part due to its flexibility in deployment (signals can be extracted anywhere two stations are present) and due to the fact that it can recover shorter wavelength surface waves than is observed with distant earthquakes. While the earthquake-based work of Lin, Tsai, and Ritzwoller (2012) recovered signals at periods in the range of 24 to 100 s, the ambient noise signals extracted in this paper are in the range of 8 to 32 s, allowing crustal properties to be probed at both shallower ranges and higher resolution.

We favor the wavefront tracking method for two reasons. The first reason is that it properly accounts for energy focusing and defocusing, which may be a significant contribution to differences in observed amplitudes. Second, and important uniquely for the ambient noise data used in this paper, we prefer the method because the interpretation and the use of raw amplitude information from the ambient noise wavefield have been a topic of some debate. Analytic work (e.g., Tsai, 2011; Weaver, 2011a), numerical simulations (e.g., Cupillard & Capdeville, 2010), and observations (e.g., Ermert, Villaseñor, & Fichtner, 2016) all point to the fact that the amplitudes of noise correlation functions (NCFs) are highly dependent on the distribution of noise sources. As Snieder (2004), Tsai (2010), and others show, the waveform recovered by noise correlation will be a true and accurate Green's function between the two stations if and only if the background noise field is equally partitioned in time, space, frequency, and mode. This constraint is obviously not met in the real Earth, where dominant noise sources are strongly related to water-wave interactions in the oceans (i.e., Longuet-Higgins, 1950).

Various signal processing techniques may be employed to mitigate these nonstationary biases (e.g., Bensen et al., 2007), but many such techniques unfortunately leave an NCF signal arbitrarily normalized, hindering the ability to make relative amplitude measurements. Further, such processing affects the sensitivity kernels of an NCF (i.e., Fichtner et al., 2016), making it difficult to properly attribute the effect of such processing without complete knowledge of the background noise field. The full-waveform interferometry described by Fichtner et al. (2016) may offer an approach that can simultaneously describe both sources and structures, but this is difficult to apply in practice since solving for the full 3-D ambient noise source distribution is a highly underdetermined inverse problem. By all accounts of ambient noise theory, the raw amplitude measured of an NCF should not be trusted to give reliable measures of structure alone.

Despite these theoretical problems with amplitude measurements, other studies have advocated that the use of raw NCF waveforms is acceptable in some cases. Prieto et al. (2009) and Lawrence and Prieto (2011) were able to recover reasonable attenuation measurements from the western U.S. by measuring waveform coherency and, in separate work, argue that any directional source biases are negligible (i.e., Lawrence et al., 2013), especially for a method where measurements can be averaged over a wide range of station-station azimuths. Additionally, scattering from crustal heterogeneities is expected to redistribute energy and mitigate some of these biases, especially at shorter wavelengths (e.g., Campillo & Paul, 2003; Prieto et al., 2011). However, we reemphasize that the validity of all of these arguments is debated by Tsai (2011), Weaver (2011b), and Menon et al. (2014).

As a separate example, amplitudes of NCFs are used by Denolle et al. (2014) and Viens et al. (2016) to recover realistic basin amplification effects and are well validated with actual earthquake events. In such virtual source reconstructions, the authors are careful to only consider station-station paths over a narrow range of azimuths and are careful to stack all NCFs over a consistent time period, thus mitigating potential biases from inhomogeneous noise source distributions. Viens et al. (2017) also demonstrate that while temporal and azimuthal variations in noise source may contribute to variability in NCF amplitudes, such errors are small compared to the large effect of sedimentary basin amplifications they observe, indicating that direct observation can still be useful in some contexts.

In contrast to the above mentioned approaches, the wavefront tracking method is only concerned with how a wavefield evolves across an array; the initial distribution of seismic energy is not important. This approach has been successfully used with eikonal, Helmholtz, and amplification tomography (i.e., Lin & Ritzwoller, 2011; Lin et al., 2009; Lin, Tsai, & Ritzwoller, 2012). If one considers all NCF pairs with a given station in common and all treated with identical and linear preprocessing, the resulting wavefield will evolve with time obeying the linear wave equation (Lin et al., 2013). This wavefield need not be composed of true Green's functions, and

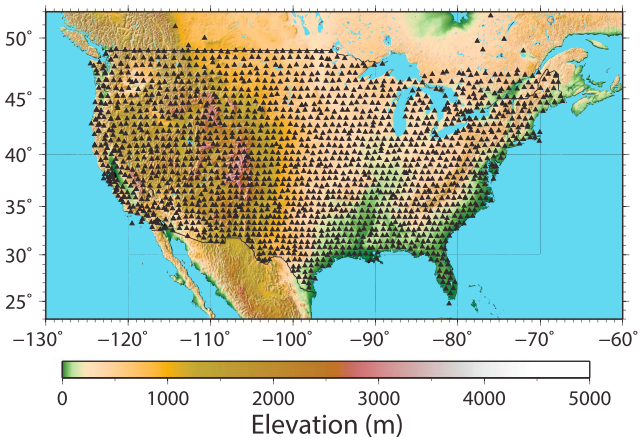

Figure 1. Stations used for ambient noise cross correlation.

although we often refer to the single common station as a "virtual source," wave energy does not and need not originate from this point. Rather, the cross-correlation operation supplies means to collect and observe wavefronts that can be used in the wavefront-tracking approach. This was the basis of similar work using ambient noise signals from a very dense array in Long Beach, CA, to recover surface wave site amplification effects at frequencies up to 1–2 Hz (i.e., Bowden et al., 2015).

This paper explores the extent to which noise amplitude information can be recovered in a wavefront tracking scheme from USArray with the strictest possible processing. Steps are taken (explained below) to ensure a relatively high signal-to-noise ratio (SNR), while treating all stations equally and making measurements only when stations can be stacked for an identical period of time. We note that the resulting surface wave amplification and attenuation maps have implications for tectonic structure and may be used in future tomographic efforts that include joint inversion of multiple data sets, though we also consider it an advantage that these properties may be directly observed without the need for complex 3-D inversions or other assumptions.

2. Methods

2.1. Ambient Noise Cross Correlations

In processing the ambient noise cross correlations, we use vertical component data from 1,901 stations between 2007 and 2014 from USArray and supplemented by Advanced National Seismic System (ANSS) and regional networks, shown in Figure 1. We divide data into day-long segments of time, with the same preprocessing approach as in Bowden et al. (2015). This uses a modification of traditional spectral whitening (i.e., Bensen et al., 2007) that weights the spectra of all stations for a given day by a single, representative spectrum constructed by taking the 95th percentile at each frequency for all station spectra on that day, and this single spectrum is subsequently smoothed. Similarly, a version of time domain weighting is used that scales the amplitudes of all resulting NCFs from a single day by a single, common factor before including each in a cumulative monthly stack, determined by taking the 95th percentile of the peak amplitudes of all NCFs. In this way, a set of spurious measurements from a day biased by earthquakes would not be more strongly weighted than any other day. These "whole-array" processing steps are not as effective as traditional preprocessing techniques at producing clear arrivals (i.e., Bensen et al., 2007), but they do ensure that relative amplitude information is preserved and the wave equation still holds (e.g., Lin et al., 2013). The more traditional versions of spectral whitening or time domain normalization act on each station individually, resulting in waveforms that are arbitrarily normalized relative to one another, and should not be applied when amplitudes are of interest. An alternative approach would simply be to not use any preprocessing whatsoever, but we find the SNR of our measurements is too poor in this case (such that the NCFs do not converge fast enough).

Stations in USArray were rolled across the U.S. from west to east between 2004 and 2014. At any given time, a smaller number of stations were concurrently recording (each station was in the ground for roughly 18 months), and most of these were focused over a narrow range of longitudes. This poses an additional difficulty in preserving relative amplitude information: we are only able to directly compare amplitudes of stations pairs that were stacked over an identical time window. To account for this, we divide the continental U.S. into 1,115 subregions of roughly 600 km by 600 km in size, evenly distributed with significant overlap (up to 85% of a subregion overlaps with neighbors for the interior of the U.S.). This size is somewhat arbitrary, but we find that a 600 km wide subregion from USArray generally has stations in the ground simultaneously for a reasonable period of time. A wavefield across each subregion is constructed using cross correlations from all stations within a given subregion against any possible virtual source (i.e., any station), with the NCFs stacked for an identical number of months. Stations within the subregion are also counted as possible virtual sources. An example of one such subregion is shown in Figures 2a and 2b, and we note that while the time period of months used for the NCFs in Figure 2a is different than those in Figure 2b, within each set of observations the months used for stacking remain consistent.

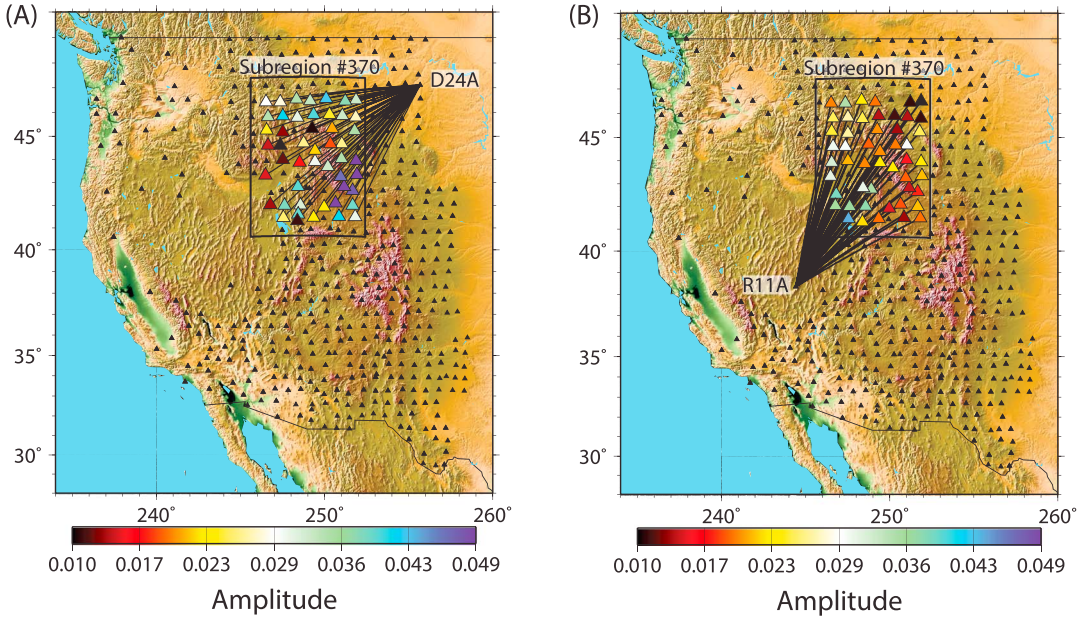

Figure 2. One example subregion or subset of stations. A given external virtual noise source must be stacked over an identical period of time, though this time period may be different for each external virtual noise source (black triangles). (a) D24A as the virtual source. (b) R11A as the virtual source.

Also, because stations are occasionally missing short periods of data, we do allow a station that was online for 90% of a given month to still be considered complete in regards to this stacking (though each station is properly weighted by the number of days it was present). On average, we are able to stack each station-to-subregion set for 3 months, though in some cases the stations were arranged such that more than a year's worth of data could be collected and consistently stacked. This difference in stacking durations makes for vastly different signal-to-noise ratios (SNR) in the recovered NCF waveforms, but we are careful to reject any NCF with an SNR less than 6, defined as the peak amplitude within the expected surface wave arrival window to the RMS of the trace outside of the expected arrival window.

This process of subdividing the array into many subregions could, in theory, introduce some amount of spatial bias or aliasing due to the overlapping nature of subregions. However, if a given location in the area is sampled by multiple overlapping regions, this simply means that more observations of the wavefront are available (as explained in more detail below). In our final measurements, we observe no bias or pattern resembling the initial distribution of subregions and so are confident that this is not an issue. Unfortunately, much of the potential data is discarded in this strict stacking procedure, but this is preferable to dealing with the unknown effects of stacking over uneven time windows.

2.2. Wavefront Tracking Across a Given Subarray

Once noise correlations are complete, we can proceed with the wavefront tracking approach of Lin, Tsai, and Ritzwoller (2012), in a manner that is (nearly) independent of the wavefield source or type. The method considers the amplitude, $A(x, y)$, and phase travel time, $\tau(x, y)$, of an assumed 2-D surface wavefield at a given period—in this case the vertical component of Rayleigh waves at numerous locations throughout a given subarray, extracted from waveforms with standard frequency-time analysis (i.e., Levshin & Ritzwoller, 2001). Fundamental-mode Rayleigh waves are isolated by the analysis' requirement that a clear dispersion branch is observed and by requiring a signal-to-noise ratio of the arrival compared to other signals of at least 6. It is assumed that there is only one observed wavefront originating at the virtual source station. The amplitudes (for example, from Figures 2a and 2b) and travel times are used to construct maps of $A(x, y)$ and $\tau(x, y)$ by fitting a surface onto a fine, regularly spaced grid with spacing of 0.2° latitude and longitude. This surface fitting procedure is done using the minimum-curvature surface subroutine of GMT (Wessel et al., 2013) and is usually quite successful at describing the evolution of a wavefield as long as the wavelength used is not

shorter than the average station spacing. Automated quality control checks are used to correct for a 2π ambiguity in measuring phase velocity.

As described by Lin, Tsai, and Ritzwoller (2012), surface waves in 3-D can be described at the Earth's surface by 2-D surface wave potentials as long as lateral velocity variations are relatively smooth. The potential $\chi_{2\text{-D}}(x, y, t)$, in this case for the vertical component of Rayleigh waves, is related to observed amplitudes of the wavefield, $A(x, y)$, by

$$A(x,y)e^{i\omega(t-\tau(x,y))} = \beta(x,y)\chi_{2\text{-D}}(x,y,t) \tag{1}$$

where $\beta(x, y)$ is a local, relative amplification term for surface wave potentials (discussed more below). This potential satisfies the 2-D wave equation (e.g., Tromp & Dahlen, 1992), which leads to the following equation, also sometimes referred to as the transport equation

$$\frac{2\nabla\beta\cdot\nabla\tau}{\beta} - \frac{2\alpha}{c} + S = \frac{2\nabla A\cdot\nabla\tau}{A} + \nabla^2\tau \tag{2}$$

where α relates to attenuation and c is phase velocity. All variables in equation 2 have a spatial dependence on (x, y), but this is omitted in equation 2 (and most of the paper) for brevity. The term α refers to intrinsic attenuation and relates to the more commonly used Q factor by $\alpha = \pi f/(UQ)$ where f is frequency and U is group velocity (e.g., Mitchell, 1995; Yang & Forsyth, 2008), and attenuation is assumed weak enough to not affect phase travel time. Compared to the derivation of Lin, Tsai, and Ritzwoller (2012) and following Bowden et al. (2015), we use a more general solution in which a generic source term, $S(x, y)$, is included and described later.

Equation 2 tracks changes in amplitude as the Rayleigh wave propagates from one region to another. It is arranged in such a way that the right-hand side consists entirely of observables A and τ. Qualitatively, equation 2 can be described in the following way: observations of spatial amplitude changes in the direction of wave propagation ($\nabla A \cdot \nabla\tau$) are corrected by the amplitude changes associated with the wavefront's changing shape and velocity, including geometric spreading, wavefront focusing, and a shift in wavelength from one medium to another (all captured by the $\nabla^2\tau$ term). Following Lin, Tsai, and Ritzwoller (2012), this sum on the right-hand side is referred to as "corrected amplitude decay," and such maps are collected for each virtual source available to each subregion at a range of discrete periods, from 8 to 32 s. The sum of these two terms on the right-hand side would be zero in the absence of geologic variations causing amplification, attenuation, or additional seismic sources (all pieces of the left-hand side). These three terms can be further decoupled by noting that the amplification caused by underlying geologic structure will depend on the direction of propagation ($\nabla\beta \cdot \nabla\tau$), while attenuation or simple sources will act on a wavefront isotropically.

Here we use observations of A and τ that are specifically for a single period of the vertical component of fundamental-mode Rayleigh waves. This fundamental mode was selected and isolated in the frequency-time analysis used, but we note that the method could be applied to higher modes if these were well observed. To use horizontal-component Rayleigh or Love observations, an additional gradient or curl term, respectively, is needed to relate observed amplitude to the conserved surface wave potential (Tromp & Dahlen, 1992). This is feasible under the framework of this method, but it is not the focus of this paper.

For the amplification term, there are two possible ways to define and interpret this, and the difference is not well described in the literature. In equation 2, β refers to a surface wave potential amplification factor that results from the wavefront tracking observations. This can be expressed as a ratio of measurements between a reference site (indicated by superscript R) and any other site of interest as

$$\beta = \left(\frac{cUI_0}{c^R U^R {I_0}^R}\right)^{-1/2} \tag{3}$$

where c is phase velocity, U is group velocity, I_0 is an integral over the surface wave eigenfunctions (e.g., Lin, Tsai, & Ritzwoller, 2012; Tromp & Dahlen, 1992). For Rayleigh waves the I_0 integral is defined as

$$I_0 = \int_0^\infty \rho(z)\left(u_1(z)^2 + u_2(z)^2\right)\mathrm{d}z \tag{4}$$

where $\rho(z)$ is the density as a function of depth, and $u_1(z)$ $u_2(z)$ describe the normalized horizontal and vertical eigenfunctions, respectively. The ratio of phase velocities (c/c_R) in equation 3, specifically, is important because the $\nabla^2\tau$ term in equation 2 corrects for shifts in wavelength in addition to geometric spreading,

focusing, and defocusing of a wavefront. In this wavefront tracking approach, the $\nabla^2\tau$ term from equation 2 is necessary to account for 2-D geometric effects in a proper finite-frequency theory. Presenting observations of β defined this way is the most natural for this work, and β is referred to as "observed amplification" throughout this paper.

However, since the amplification β is relative to the surface wave potential, and the potential is not directly observable, it is not the appropriate amplification factor to directly describe observed surface wave amplitudes. To properly describe changes in a surface wave's amplitude that will be observed due to site effects related to the local 1-D geological structure, a different site-amplification factor (i.e., Bowden & Tsai, 2017; De Noyer, 1961; Tsai et al., 2017) can be defined as

$$\frac{A_n}{A_n{}^R} = \left(\frac{UI_0}{U^R I_0{}^R}\right)^{-1/2} \tag{5}$$

where A_n and $A_n{}^R$ describe the amplitudes of a surface wave at a given site and reference site as a function of frequency, respectively. (Note that the difference between equation 5 and equation 3 is that equation 3 contains an extraphase velocity term.) This version of site amplification applies directly to the amplification of observed displacement amplitudes as a surface wave travels from one 1-D profile to another and therefore may be most useful for descriptions of site response for hazard purposes. This definition is also the more appropriate version of site amplification to use for methods such as that of Eddy and Ekström (2014) that rely on more direct observations of amplitude ratios without accounting for geometric focusing and defocusing of the wavefront. Again, we refer to β as defined in equation 3 as observed amplification for the wavefront tracking method (i.e., Bao et al., 2016; Lin, Tsai, & Ritzwoller, 2012, and this work), but this difference should be kept in mind when interpreting the results.

Once the spatial gradients on the right-hand side of equation (1) have been measured, the corrected amplitude decay depends only on the direction of wave propagation and geologic structure, rather than any time-varying properties of the far-field ambient noise field. Thus, different azimuths of wave propagation may be compared even though the time range of data used may be different. Additionally, measurements from different subregions may now be collected for regions of overlap; all observations of corrected amplitude are treated equally, regardless of virtual source or subregion. Collecting observations in regions of overlap may lead to some redundancy of any given source-station pair, but we believe this has little effect on the resulting analysis. As in Lin, Tsai, and Ritzwoller (2012) and Bao et al. (2016), the corrected amplitude decay measurements are plotted as a function of azimuth and a sinusoidal curve is fit with 1-psi anisotropy (that is, exactly 360° periodicity but arbitrary phase, amplitude, and static offset), as in Figure 3. Once a 1-psi curve is fit, the magnitude and direction of peak amplification is attributed to the term $(2\nabla\beta \cdot \nabla\tau)/\beta$, while the static offset is attributed to the isotropic attenuation and source terms. This curve-fitting approach is also discussed and preferred by Bao et al. (2016) over an approach that measures attenuation and amplification through separate approaches. One example from near the Yellowstone Hotspot below (Figure 3a) exhibits a high amount of directionally dependent amplification, while the other example from the Basin-and-Range Province (Figure 3b) does not.

We note that we keep the acausal (negative time lag, inwardly propagating) and causal (positive time lag, outwardly propagating) sides of the NCF separate to distinguish between the effect of attenuation and sources. New energy contributed to the system within a given subregion (referred to as S in equation 2), either from new ambient noise sources or energy scattered away from heterogeneities that act as new isotropically radiating sources (i.e., Ma & Clayton, 2014), will primarily only affect the acausal incoming wavefront (Bowden et al., 2015; Liu, Ben-zion, & Zigone, 2015). This is because the region of noise sources that most strongly contributes to the NCF is changing along with the incoming wavefront, while for the outgoing wavefront the influential noise sources are relatively fixed somewhere at or behind the virtual source. Because the positive-lag, outwardly propagating wavefront is assumed to be affected by attenuation only (and not sources), we extract our observations of attenuation from these measurements only. Comparing the incoming and outgoing wavefronts may yield constraints on sources and scatterers, but because we cannot distinguish between sources and scatterers we do not interpret these results here.

Because of this difference in causal and acausal time lags, we perform the 1-psi fits in three successive steps. For a first pass, both the causal and acausal corrected amplifications are considered together, and the best fitting 1-psi amplitudes and directions are determined, allowing for variable amplification magnitude, direction, and static offset (the black curves in Figures 3a and 3b). Combining causal and acausal measurements

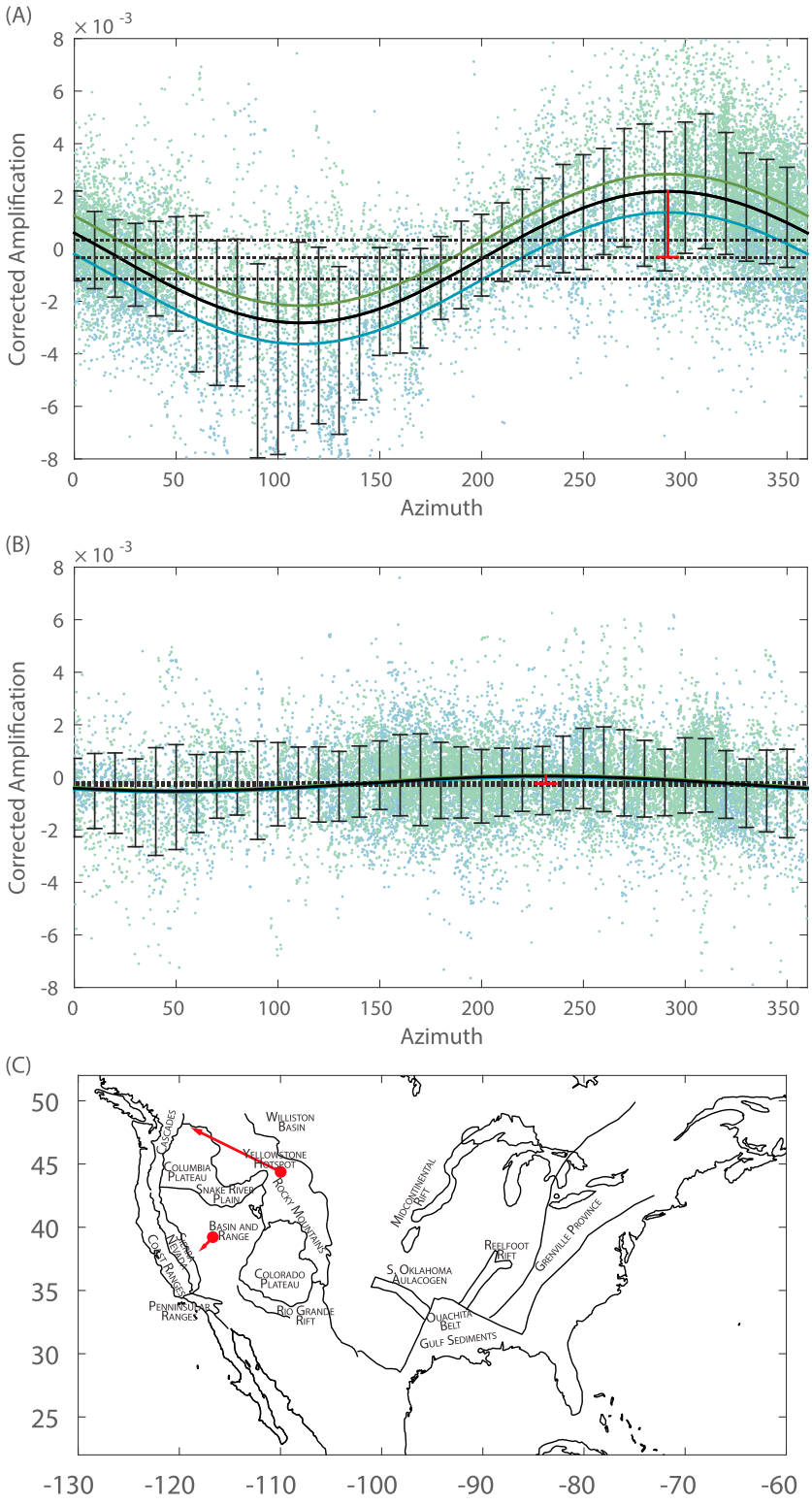

Figure 3. Example corrected amplification measurements as a function of propagation azimuth at 24 s period. Each green or blue dot represents the incoming or outgoing observation from a virtual source. One point exhibits strong amplitude effects and is near the (a) Yellowstone hotspot, and the (b) other example point in the relatively homogenous Basin-and-Range Province does not. For both measurements, the location, magnitude, and direction of the 1-psi curve is represented as a vector in the (c) map view. Geologic and tectonic provinces referred to throughout the paper are labeled in the map (Figure 3c).

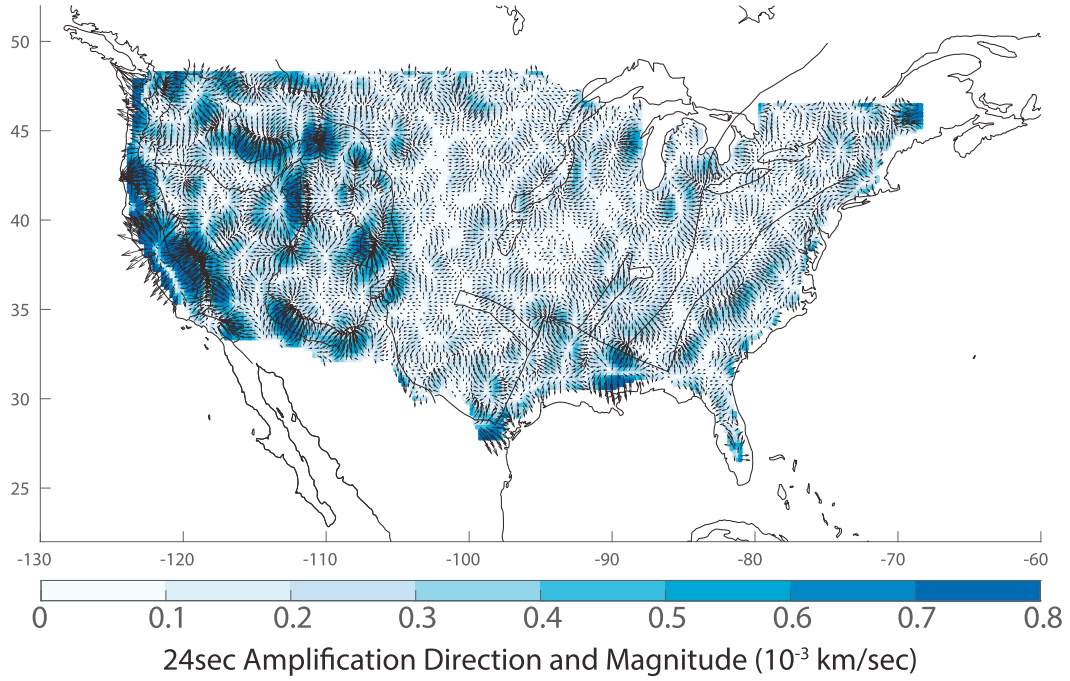

Figure 4. Map view of all 1-psi magnitudes and directions for 24 s Rayleigh waves. Stronger colors indicate a stronger gradient in observed amplitudes, which is expected to correlate with boundaries of geologic provinces.

is advantageous because some regions of the U.S. exhibit very few measurements of one or the other (e.g., near the edges or coastlines), but using both allows for a more complete range of azimuthal observations and a more robust fit. With the amplification directions and magnitudes constrained and fixed, a second iteration is then performed to find the best fitting static offsets separately for the causal and acausal waves. As described in the previous paragraph, our measurements of attenuation are derived only from the outgoing, causal wavefield. Finally, these static offsets (dashed lines in Figures 3a and 3b) are subtracted from each individual corrected amplification measurement (the blue and green dots in Figures 3a and 3b) such that both incoming and outgoing wavefronts are unbiased by attenuation, scattering, or sources, and then a final measurement of amplification direction and magnitude is made. All measurements at a given location are discarded if the mean chi-squared misfit measured at each of 18 different 20° azimuthal bins (shown in Figure S1 in the supporting information) is greater than 0.1 (see supporting information), which was most often the case only at the edges of USArray. Areas with a high uncertainty within the interior of the array are also excluded, but these are generally small and effectively smoothed over in the process of fitting amplification measurements. Figure 4 shows the lateral pattern of these best fitting magnitudes and directions for 24 s Rayleigh waves.

Given maps like Figure 4 at each discrete period, we can finally describe the observed amplification term, β. The vector field of maximum amplification magnitude and direction is attributed to the $(2\nabla\beta \cdot \nabla\tau)/\beta$ term in equation 2, and following Lin, Tsai, and Ritzwoller (2012), the best fitting scalar amplification map, β, is determined through a linearized fit to the vector field. Unlike the work of Lin, Tsai, and Ritzwoller (2012), no successive iterations of the entire method is performed; one such iteration was tested, but the change was negligible enough and the computational cost high enough that it was considered unnecessary. Finally, although most of this processing is performed on a regular grid of 0.2°, we note that the actual resolution of attenuation and amplification depends on the original station spacing, and so features of all maps are smooth on the order of 100 km.

3. Results and Discussion

3.1.1. Amplification Maps

Final observed surface wave amplification (β) maps are presented in Figure 5, at periods of 8, 12, 16, 24, and 32 s. For each map, the reference value for β (i.e., β = 1) is arbitrary and is taken simply as the point

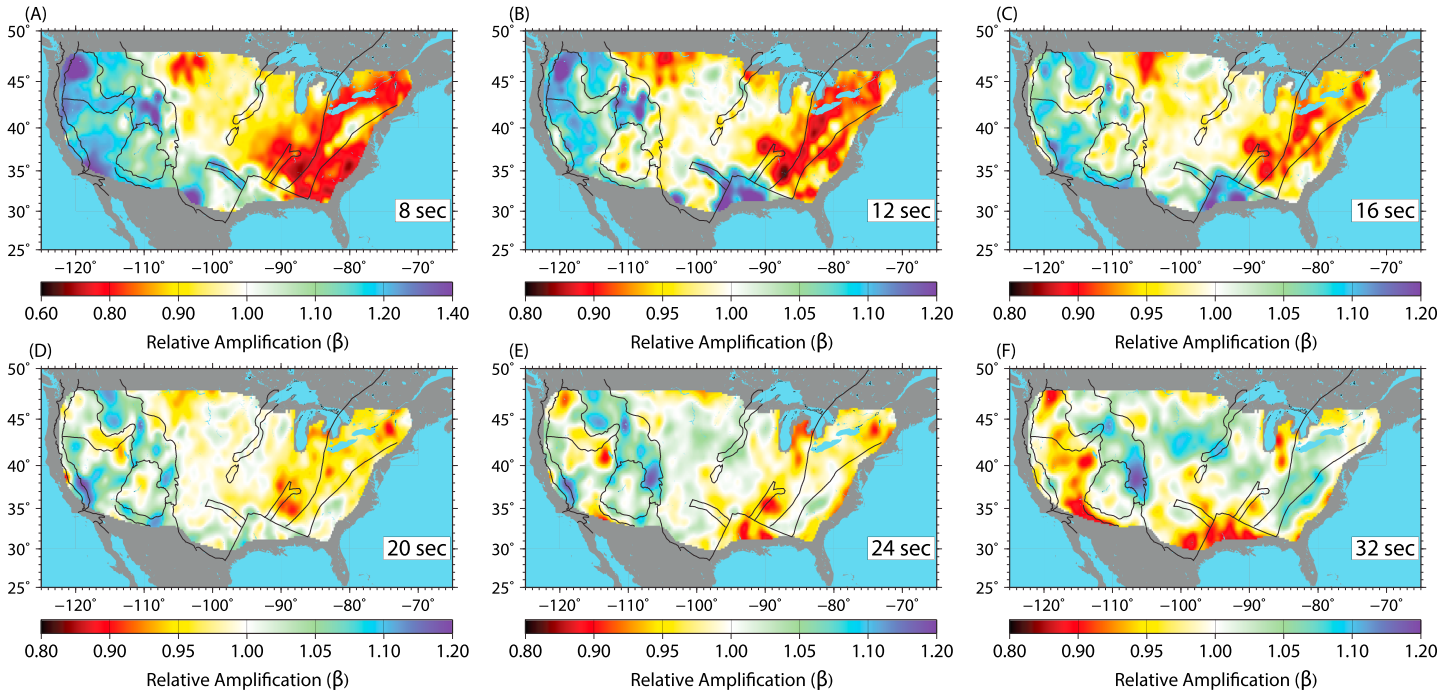

Figure 5. Amplification measurements (β) at a range of periods: (a) 8, (b) 12, (c) 16, (d) 20, (e) 24, and (f) 32 s. We note that all maps are plotted with a nonlinear color scale to emphasize differences closer to 1. Only the 8 s (Figure 5a) is plotted with a different scale than the others.

representing an average. Any map could be renormalized and its colorbar shifted arbitrarily. As mentioned previously, this amplification is most appropriate for wavefront tracking approaches (e.g., Bao et al., 2016; Lin, Tsai, & Ritzwoller, 2012), but maps of amplification β corrected for phase velocity may be most appropriate for direct amplitude observations (e.g., Eddy & Ekström, 2014), and these alternative site amplification factors based on equation 5 are presented in Figure S2.

As expected, the maps show significant correlation with known tectonic provinces such as the Snake River Plane, Colorado Plateau, Oklahoma Aulacogen, and others (see tectonic province labels in Figure 3c). Higher amplification is observed at almost all periods at the Yellowstone Hotspot, which is known to be warm and therefore has slower seismic waves (Huang et al., 2015; Seats & Lawrence, 2014), resulting in amplification. At shorter periods (i.e., 8 and 12 s, Figures 5a and 5b), the maps indicate strongest amplification in regions with known slow seismic velocities, primarily controlled by the presence of sediments such as in the Columbia Basin or in the Gulf of Mexico (e.g., Mooney & Kaban, 2010). Indeed, to first order these maps are expected to correlate with seismic velocity; surface waves entering a low-velocity sedimentary basin will be slowed and amplified. In contrast, the older and faster stable craton in the eastern U.S., including the Trans-Hudson, Grenville, and Appalachian Provinces, are associated with lower amplification, which is most obvious again at shorter periods (i.e., Figures 5a and 5b).

There is a reversal of some of the dominant lateral features as observations are extended to longer period. While the shorter period observations mentioned above were sensitive to the top 10 km of crustal material, 32 s Rayleigh waves start to be sensitive to upper mantle material (Figure 6e). Crust in regions such as the sedimentary basins in the Gulf of Mexico or regions thinned by tectonic activity such as the Basin-and-Range Province are significantly thinner and so are the first to see higher mantle velocities and the correspondingly lower amplification. In contrast, areas with the thickest known crust, such as the Southern Rockies, remain as a region of high surface wave amplification.

Figure 6 shows depth sensitivity kernels for various surface wave observables, for an average representative 1-D velocity profile for the continental U.S. from the tomography of Schmandt et al., (2015) (which will be further compared later), calculated by iteratively perturbing shear wave velocity, *P* wave velocity and density, and recording the resulting change in semianalytic predictions (using Computer Programs in Seismology; i.e., Herrmann, 2013). Standard relations from Brocher (2005) are used to infer Vp and density from the Vs profile

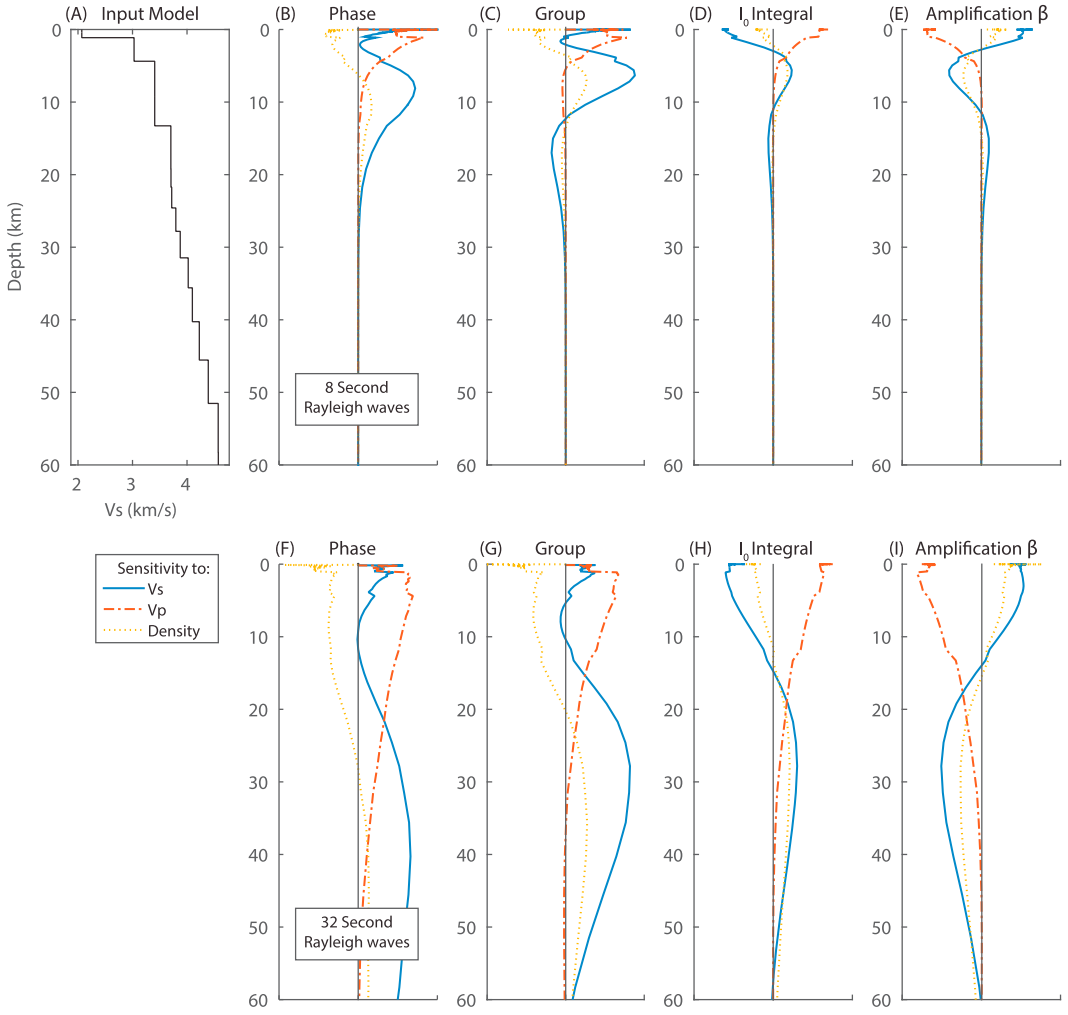

Figure 6. Sensitivity kernels for a representative 1-D velocity profile (a) at 8 and 32 s. (b–i) Sensitivity to Vs (solid blue line), Vp (red dashed line), and density (yellow dotted line) are indicated separately. The observed amplification sensitivity kernel is calculated using the phase velocity, group velocity, and I_0 energy integral kernels, following equation 3.

shown. The amplification sensitivity kernels indicate that they are sensitive to a shallower region and with opposite sign for some depths as compared to phase or group velocity, and so care should be taken if these maps are to be compared to surface wave velocity observations of other studies.

3.1.2. Amplification Comparison to Other Models

We can compare the features of these maps to 3-D models. Schmandt et al. (2015) has produced one such 3-D model using a variety of observations, from both earthquake and ambient noise dispersion, H/V curves, and teleseismic receiver functions. At each point a 1-D shear-wave velocity profile is considered, Vp and density are estimated based on standard relations (i.e., Brocher, 2005), and β semianalytically estimated using equation 3. Again, the reference site is arbitrary, and $\beta = 1$ is defined as the whole-array average.

In Figure 7, our observed amplifications at 8, 20, and 32 s are presented again next to the theoretical model predictions using the model of Schmandt et al. (2015), as well as the difference between the two. Most of the dominant lateral features are present in both maps, as well as the overall magnitude of amplification response (i.e., ±20% in many regions). However, the difference maps indicate that there remain a number of regions with differences. The most severe of these differences is observed at 32 s, where it appears that the model predicts significantly stronger amplifications in the western U.S. (indicated by a negative residual in Figure 7i). This discrepancy could indicate an issue with the velocity and density model used. Though we cannot comment on the validity of the velocity model itself or the need for improvements, we note that our model predictions rely on standard relations between Vs and Vp, as well as between Vs and density described

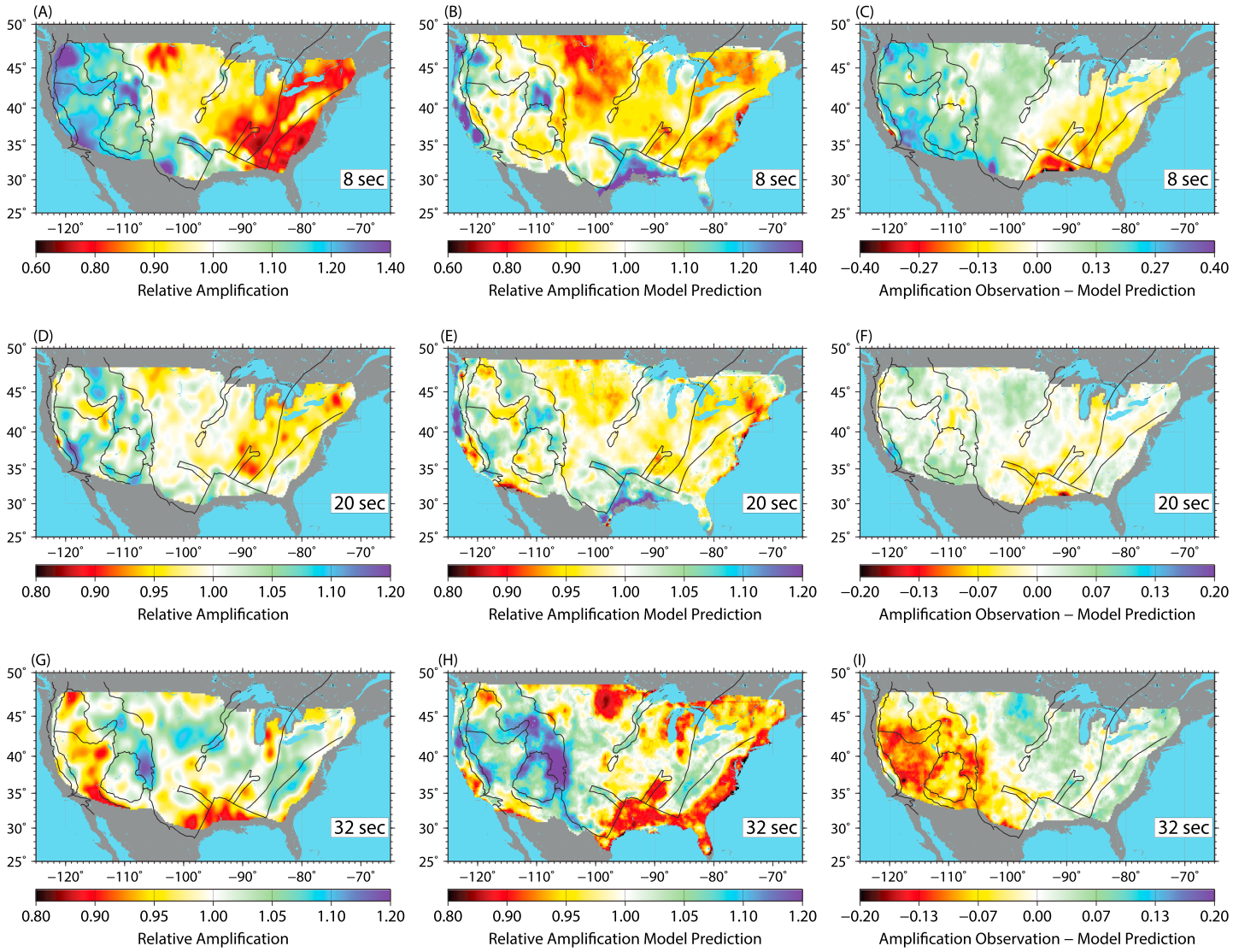

Figure 7. Comparison of our observations (a, d, g) to semianalytic model predictions (b, e, h) and the difference of the two (c, f, i) for three different periods (8 s, 20 s, and 32 s, respectively).

by Brocher (2005). These relations represent averages and were likely not intended to unilaterally represent the various rheologies found throughout the continental U.S. Considering it is the 32 s maps that are most sensitive to mantle materials, and that mantle materials are likely not well represented by the same Vp, Vs, and density relations used for the crust, we expect this is the primary reason for discrepancies between the model and our observations. Inaccuracies in the assumed Vs-Vp-density scalings may also explain differences in the shorter-period (8 s) map (Figure 7c), in that prominent features here relate more to surface geology and shallow sedimentary basins such as in the Gulf Coast. Testing alternative relations, or even constraining and improving such relations, may be an opportunity of future work with these data sets.

As a different test, we can compare our noise-derived amplification observations to the earthquake-derived observations of Lin, Tsai, and Ritzwoller (2012) (Figure 8). Again, Lin's previous work was focused on longer period measurements but at least measurements of 24 s and 32 s overlap. Here we remeasured an average, reference point of amplification for the western U.S. and rescale the relative amplifications shown in Figures 8a, 8b, 8d, and 8e for a clearer comparison once values are compared in Figures 8c and 8f. In general, we find very good agreement, with any substantial differences only near the edges of our domain. Notably, the strong discrepancy that was present between observation and model at 32 s (Figure 7i) throughout the

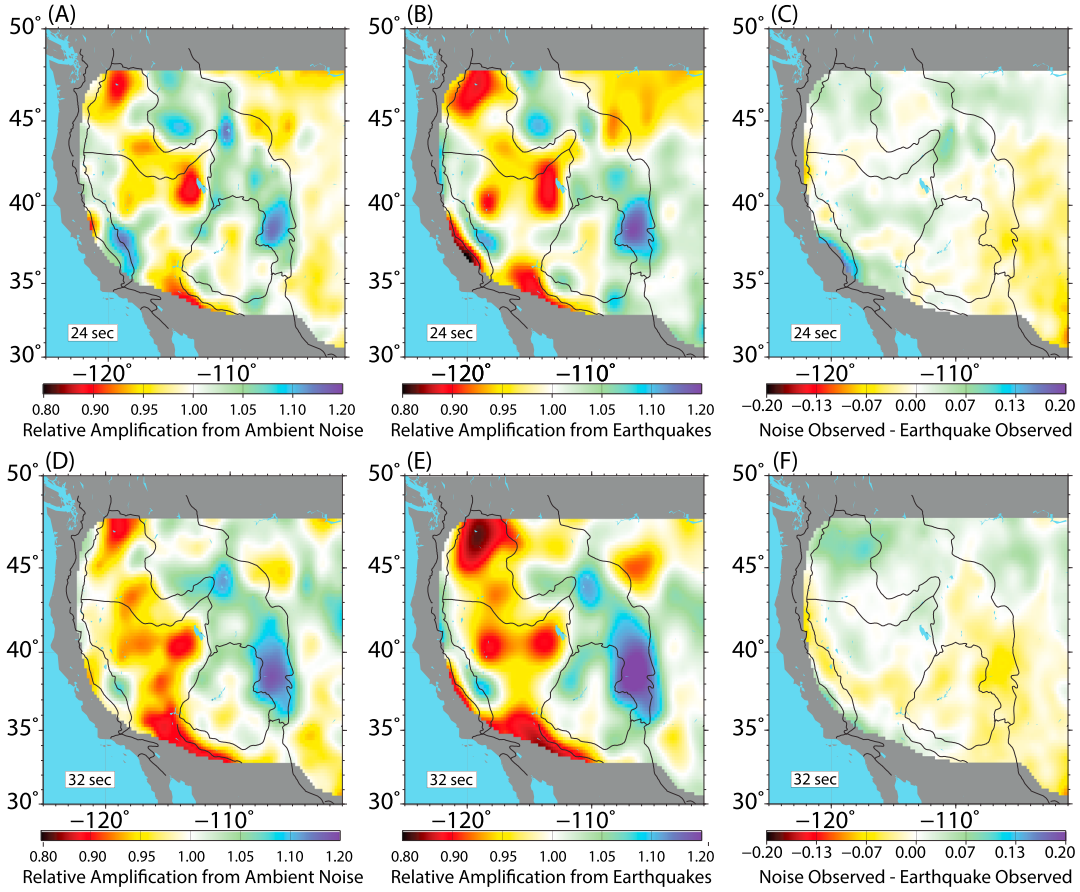

Figure 8. Our noise-derived observations of (a and d) amplification, (b and e) the earthquake-derived observations replotted from Lin, Tsai, and Ritzwoller (2012), and the (c and f) difference between the two at 24 and 32 s. Relative amplifications in Figures 8a, 8b, 8d, and 8e have all been arbitrarily rescaled by the average value for this region of the western U.S.

western U.S. is not as strong of an issue here. These similarities confirm that the ambient noise measurements do not provide different or biased information than would be inferred from earthquake wavefronts. However, it should be noted that the earthquake-based observations use similar processing and gradient measurements (i.e., equation 2), so any systematic biases in the method would appear in both maps.

We can also compare our observations to those of Eddy and Ekström (2014), who use earthquakes to observe amplitude ratios at adjacent stations. While their measurements focus on mostly longer periods (35 s to 125 s), their 35 s observations may be expected to correlate with our 32 s noise observations. Again, because their method relies on direct observation of surface wave amplitudes without a focusing and defocusing correction, a site amplification term defined as in equation 5 without phase velocity terms is most appropriate for comparison (see Figure S2). Indeed, many lateral features are consistent, with low amplification of ~0.9 in the Texas Gulf, and northern Basin and Range provinces, as well as high amplification of ~1.1 in the southern Rockies for both studies. The largest discrepancy is observed in the central northernmost part of the array at around −105 W, 48 N, where the 35 s map of Eddy and Ekström (2014) shows strong amplifications above 1.15 while our observations show little or no structure in this region.

3.2.1. Attenuation Maps

We also examine the level of intrinsic attenuation, indicated by a persistent loss of energy at a given location regardless of propagation direction (see equation 2). This is measured by a negative static offset of the 1-psi sine curve for outgoing waves. This static offset is attributed to the $-2\alpha/c$ term in equation 2, and again α can be related to a quality factor Q by $\alpha = \pi f/(CQ)$. As in the work of Bao et al. (2016) we find it necessary to smooth the maps of α using a Gaussian filter of roughly 100 km. Even though we could constrain site-specific phase and group velocities from our measurements, we use a constant phase and group velocity appropriate to the

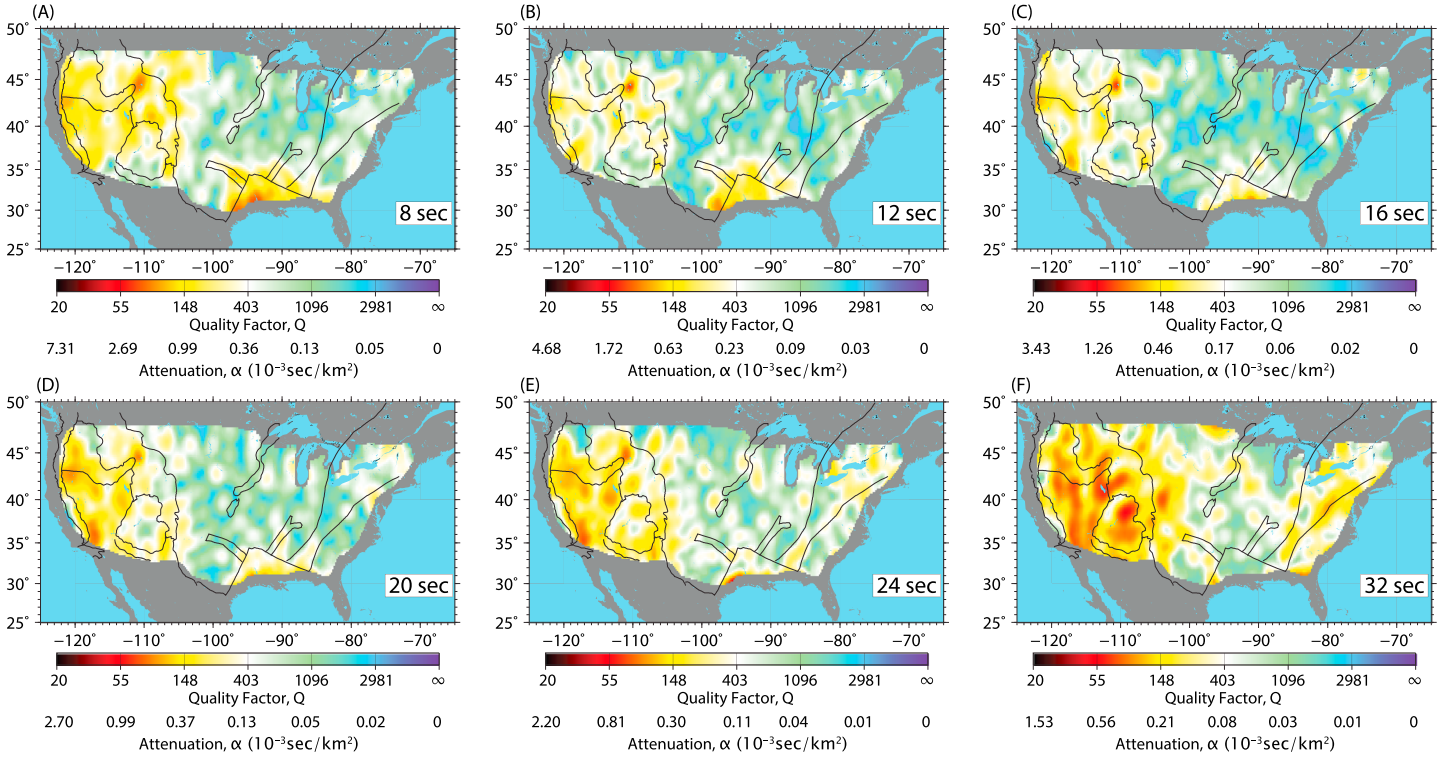

Figure 9. Attenuation observations at six different periods, again 8, 12, 16, 20, 24, and 32 s. In each plot a logarithmically spaced *Q* factor is indicated on the color scale, though we also show the corresponding conversion to attenuation coefficient, α.

period (as determined by the representative profile in Figure 6), so our observations are not complicated by different patterns of spatial variability in velocity structures. In any case, the attenuation we observe varies by nearly 2 orders of magnitude (plotted logarithmically in Figure 8), and so including a slightly different phase or group velocity will not change the salient features in any significant way. The phase velocities used as a representative average are 2.99, 3.14, 3.27, 3.39, 3.50, and 3.67 km/s for each of the six periods, respectively, and group velocities are 2.67, 2.79, 2.85, 2.90, 2.97, and 3.19 km/s, respectively. Also, we remind the reader that these measurements are for Rayleigh wave attenuation and may differ from observations of *P*, *S* or the commonly observed Lg phase, but relations for different *Q* observables have been discussed by Mitchell et al. (1976) and others.

We observe that attenuation is somewhat high at the shortest period, 8 s (Figure 9a), which is expected considering this is most sensitive to shallow crustal sedimentary basins. Even small-scale features associated with sediment fill after rifting in the Oklahoma Aulacogen, midcontinental rift and Rio Grande rift can be observed (see tectonic province labels in Figure 3c). At intermediate periods (i.e., 12–16 s, Figures 9b and 9c) attenuation reaches its lowest values (highest *Q*) in most of the continental U.S., representative of deeper crustal material. At our longest periods (i.e., up to 32 s, Figure 9f), attenuation increases again significantly, particularly in the western U.S., such as in the Basin and Range province, since these periods are now sensitive to upper mantle material. High attenuation in the Colorado Plateau and southern Rockies is unexpected, however, considering the crust should be quite thick in this region.

Throughout all periods, the Yellowstone Hotspot is prevalent as a region of high attenuation, relating to high temperatures in the magma chamber at depth (Huang et al., 2015). The high attenuation at Yellowstone is also indicative that the methodology generally works as expected. A significant static offset in the 1-psi fits (as in Figure 3a) is responsible for this reported attenuation; low velocities are expected and the corresponding high amplifications are observed, but other factors do not cause the azimuthally independent decrease in amplitude that we attribute to attenuation. As discussed by Lin, Tsai, and Ritzwoller (2012) and Bao et al. (2016) however, the focusing and defocusing effect as captured by $\nabla^2\tau$ may not be adequate on small spatial scales, and care must be taken when interpreting these results.

3.2.2. Attenuation Comparisons

Our maps can be compared to the earthquake-based attenuation maps of Lin, Tsai, and Ritzwoller (2012) and Bao et al. (2016). The 30 s attenuation map of Lin, Tsai, and Ritzwoller (2012) shows similar large-scale structure to ours at 32 s, the Basin and Range province and the southern Rockies being the most prominent features. However, Lin, Tsai, and Ritzwoller (2012) smoothed their attenuation maps with a Gaussian filter of 4°, much smoother than ours, and so further fine-scale comparisons are difficult. Bao et al. (2016) present attenuation maps at periods down to 40 s, again using a similar wavefront tracking approach, though applied to earthquake observations. Our observations at 32 s correlate well in regards to dominant lateral features and values, such as the strong difference between the western and central U.S. More specific similarities also exist, such as the slightly higher attenuation on the eastern seaboard east of the Grenville Province, the well-defined delineations of the Basin and Range Province and the Colorado Plateau, and even a small patch of higher attenuation east of the southern Rockies. Some differences exist, notably in that our observations indicate high attenuation in the Colorado Plateau not present in the maps of Bao et al. (2016).

Our attenuation maps also correlate well with expectations based on temperature observations. For example, the Southern Methodist University Geothermal Lab Heat Flow Map (Blackwell et al., 2011) based on numerous well-log and geothermal power plant measurements indicates higher temperatures in the southern Rockies, Basin-and-Range Province, Yellowstone Magma Chamber, and other places that agree with our attenuation maps at various periods, but especially in the range of 16 to 24 s. This is not surprising, considering these periods are most sensitive to the greater bulk of the crust; shorter periods may be strongly controlled by shallow compositional differences (i.e., sedimentary basins) and longer periods will begin to be affected by mantle materials.

Our maps also correlate to some extent with those of Lawrence and Prieto (2011). Their maps use a different method that has been much debated in the literature (as described in section 1), yet we see a correlation with features in the western U.S., as well as an overall trend of attenuation strength as a function of period. For example, the lateral patterns of high attenuation near the Yellowstone Hotspot, low attenuation near the boundary of the Colorado Plateau, and some high attenuation in the Mojave Desert on the southeast edge of the Sierra Nevada Range are all consistent between both methods at 24 s. However, the strength of attenuation reported is very different, with values of attenuation coefficient near $\alpha = 3 \cdot 10^{-3}$ km^{-1} near Yellowstone and the Mojave at 24 s, compared with our values of near $\alpha = 0.4 \cdot 10^{-3}$ km^{-1} at those same locations. Some other differences remain as well, such as northeast of the Basin-and-Range Province for which we observe high attenuation, but the Lawrence and Prieto observations show none (at 24 s). Our maps are, admittedly, presented with lower resolution than the Lawrence and Prieto results, but for various methodological reasons we are more confident in the wavefront tracking observations. The maps from Lawrence and Prieto, for example, use different assumptions about the background noise model (as mentioned in section 1) and do not account for focusing and defocusing of energy or local amplification as our wavefront tracking approach does. Thus, although the method of Lawrence and Prieto may lead to some reasonable lateral patterns of attenuation structure, their methods and assumptions may introduce significant bias in their quantitative results.

4. Conclusions

This paper demonstrates that tracking the amplitudes of wavefronts derived from ambient noise correlations yields expected and consistent measurements. As long as one is careful with the processing and stacking of ambient noise correlations, the evolution of a wavefield derived from an ambient noise virtual source behaves just as for earthquake sources, even when true Green's functions are not obtained. Demonstration of this functionality from USArray data, which is well understood tectonically and previously studied using earthquake-based measurements, paves the way for similar array-based approaches to continue in the future at other scales and periods, as was used on a city-scale dense array in Long Beach, CA (Bowden et al., 2015).

The surface wave amplification and attenuation maps derived here complement the longer period maps from Lin, Tsai, and Ritzwoller (2012), Eddy and Ekström (2014), and Bao et al. (2016), with observations extending down to 8 s period and providing an additional observable for the shallower regions of the crust. The maps show reasonable correlation with known tectonic and velocity structure, and any subtle differences may be used in the future to better constrain velocity structure, Vp/Vs or density relations. In the future, joint inversions should also be possible, using these measurements to complement existing observations of phase velocity, group velocity, H/V ratios, receiver functions, and others.

Finally, the surface wave attenuation maps presented here provide some of the highest resolution and most complete coverage of the crust in the continental U.S. They correlate well with known surface temperature anomalies and may be used in the future to constrain such properties as fluid content or temperature at depth. Alternatively, they provide empirical observations that may be directly used in hazard studies or other types of waveform estimation where surface waves are important.

Acknowledgments
Data from USArray were downloaded from the IRIS Data Management Center at http://www.iris.edu/hq/. The velocity model of Schmandt et al. (2015) was downloaded from IRIS at http://ds.iris.edu/ds/products/emc-us-crustvs-2015/. Amplification and attenuation maps are included as supporting information, and other results are available upon request to dbowden@caltech.edu. This work was supported by EAR-1453263 and EAR-1252191. F.-C. L. was supported by NSF grant CyberSEES-1442665 and the King Abdullah University of Science and Technology (KAUST) under award OCRF-2014-CRG3-2300.

References

Bao, X., Dalton, C. A., Jin, G., Gaherty, J. B., & Shen, Y. (2016). Imaging Rayleigh wave attenuation with USArray. *Geophysical Journal International*, *206*(1), 241–259. https://doi.org/10.1093/gji/ggw151

Bensen, G. D., Ritzwoller, M. H., Barmin, M. P., Levshin, a. L., Lin, F., Moschetti, M. P., … Yang, Y. (2007). Processing seismic ambient noise data to obtain reliable broad-band surface wave dispersion measurements. *Geophysical Journal International*, *169*, 1239–1260. https://doi.org/10.1111/j.1365-246X.2007.03374.x

Blackwell, D., Richards, M., Frone, Z., Ruzo, A., Dingwall, R., & Williams, M. (2011). Temperature at depth maps for the conterminous U.S. and geothermal resource estimates. *Geothermal Resources Council Transactions*, *35*, 1545–1550.

Bowden, D. C., & Tsai, V. C. (2017). Earthquake ground motion amplification for surface waves. *Geophysical Research Letters*, *44*, 121–127. https://doi.org/10.1002/2016GL071885

Bowden, D. C., Tsai, V. C., & Lin, F. C. (2015). Site amplification, attenuation, and scattering from noise correlation amplitudes across a dense array in Long Beach, CA. *Geophysical Research Letters*, *42*, 1360–1367. https://doi.org/10.1002/2014GL062662

Brocher, T. M. (2005). Empirical relations between elastic wavespeeds and density in the Earth's crust. *Bulletin of the Seismological Society of America*, *95*, 2081–2092. https://doi.org/10.1785/0120050077

Campillo, M., & Paul, A. (2003). Long-range correlations in the diffuse seismic coda. *Science*, *299*(5606), 547–549. https://doi.org/10.1126/science.1078551

Cupillard, P., & Capdeville, Y. (2010). On the amplitude of surface waves obtained by noise correlation and the capability to recover the attenuation: A numerical approach. *Geophysical Journal International*, *181*, 1687–1700. https://doi.org/10.1111/j.1365-246X.2010.04586.x

Dalton, C. A., & Ekström, G. (2006a). Constraints on global maps of phase velocity from surface-wave amplitudes. *Geophysical Journal International*, *167*, 820–826. https://doi.org/10.1111/j.1365-246X.2006.03142.x

Dalton, C. A., & Ekström, G. (2006b). Global models of surface wave attenuation. *Journal of Geophysical Research*, *111*, B05317. https://doi.org/10.1029/2005JB003997

De Noyer, J. (1961). The effect of variations in layer thickness on Love waves. *Bulletin of the Seismological Society of America*, *51*(2), 227–235.

Denolle, M. A., Dunham, E. M., Prieto, G. A., & Beroza, G. C. (2014). Strong ground motion prediction using virtual earthquakes. *Science*, *343*(6169), 399–403. https://doi.org/10.1126/science.1245678

Eddy, C. L., & Ekström, G. (2014). Local amplification of Rayleigh waves in the continental United States observed on the USArray. *Earth and Planetary Science Letters*, *402*(C), 50–57. https://doi.org/10.1016/j.epsl.2014.01.013

Ekström, G. (2014). Love and Rayleigh phase-velocity maps, 5-40 s, of the western and central USA from USArray data. *Earth and Planetary Science Letters*, *402*(C), 42–49. https://doi.org/10.1016/j.epsl.2013.11.022

Ermert, L., Villaseñor, A., & Fichtner, A. (2016). Cross-correlation imaging of ambient noise sources. *Geophysical Journal International*, *204*(1), 347–364. https://doi.org/10.1093/gji/ggv460

Ferreira, A. M. G., & Woodhouse, J. H. (2007). Source, path and receiver effects on seismic surface waves. *Geophysical Journal International*, *168*, 109–132. https://doi.org/10.1111/j.1365-246X.2006.03092.x

Fichtner, A., Stehly, L., Ermert, L., & Boehm, C. (2016). Generalised interferometry—I. Theory for inter-station correlations. *Geophysical Journal International*, *208*(2), 603–638. https://doi.org/10.1093/gji/ggw420

Herrmann, R. B. (2013). Computer programs in seismology: An evolving tool for instruction and research. *Seismological Research Letters*, *84*(6), 1081–1088. https://doi.org/10.1785/0220110096

Huang, H., Lin, F., Schmandt, B., Farrell, J., Smith, R. B., & Tsai, V. C. (2015). The Yellowstone magmatic system from the mantle plume to the upper crust. *Science*, *348*(6236), 773–776. https://doi.org/10.1126/science.aaa5648

Jin, G., & Gaherty, J. B. (2015). Surface wave phase-velocity tomography based on multichannel cross-correlation. *Geophysical Journal International*, *201*(3), 1383–1398. https://doi.org/10.1093/gji/ggv079

Karato, S. (1993). Importance of anelasticity in the interpretation of seismic tomography. *Geophysical Research Letters*, *20*(15), 1623–1626. https://doi.org/10.1029/93GL01767

Kumar, P., Kind, R., Yuan, X., & Mechie, J. (2012). USArray receiver function images of the lithosphere-asthenosphere boundary. *Seismological Research Letters*, *83*, 486–491. https://doi.org/10.1785/gssrl.83.3.486

Lawrence, J. F., Denolle, M., Seats, K. J., & Prieto, G. A. (2013). A numeric evaluation of attenuation from ambient noise correlation functions. *Journal of Geophysical Research: Solid Earth*, *118*, 6134–6145. https://doi.org/10.1002/2012JB009513

Lawrence, J. F., & Prieto, G. A. (2011). Attenuation tomography of the western United States from ambient seismic noise. *Journal of Geophysical Research*, *116*, B06302. https://doi.org/10.1029/2010JB007836

Levshin, A. L., & Ritzwoller, M. H. (2001). Automated detection, extraction, and measurement of regional surface waves, edited by A. L. Levshin and M. H. Ritzwoller. *Pure and Applied Geophysics*, *158*(8), 1531–1545. https://doi.org/10.1007/978-3-0348-8264-4_11

Liang, C., & Langston, C. A. (2009). Wave gradiometry for USArray: Rayleigh waves. *Journal of Geophysical Research*, *114*, B02308. https://doi.org/10.1029/2008JB005918

Lin, F.-C., Li, D., Clayton, R. W., & Hollis, D. (2013). High-resolution 3D shallow crustal structure in Long Beach, California: Application of ambient noise tomography on a dense seismic array. *Geophysics*, *78*(4), Q45–Q56. https://doi.org/10.1190/geo2012-0453.1

Lin, F.-C., & Ritzwoller, M. H. (2011). Helmholtz surface wave tomography for isotropic and azimuthally anisotropic structure. *Geophysical Journal International*, *186*, 1104–1120. https://doi.org/10.1111/j.1365-246X.2011.05070.x

Lin, F.-C., Ritzwoller, M. H., & Snieder, R. (2009). Eikonal tomography: Surface wave tomography by phase front tracking across a regional broad-band seismic array. *Geophysical Journal International*, *177*, 1091–1110. https://doi.org/10.1111/j.1365-246X.2009.04105.x

Lin, F. C., Schmandt, B., & Tsai, V. C. (2012). Joint inversion of Rayleigh wave phase velocity and ellipticity using USArray: Constraining velocity and density structure in the upper crust. *Geophysical Research Letters*, *39*, L12303. https://doi.org/10.1029/2012GL052196

Lin, F.-C., Tsai, V. C., & Ritzwoller, M. H. (2012). The local amplification of surface waves: A new observable to constrain elastic velocities, density, and anelastic attenuation. *Journal of Geophysical Research*, *117*, B06302. https://doi.org/10.1029/2012JB009208

Lin, F. C., Tsai, V. C., & Schmandt, B. (2014). 3-D crustal structure of the western United States: Application of Rayleigh-wave ellipticity extracted from noise cross-correlations. *Geophysical Journal International*, *198*(2), 656–670. https://doi.org/10.1093/gji/ggu160

Liu, X., Ben-zion, Y., & Zigone, D. (2015). Extracting seismic attenuation coefficients from cross-correlations of ambient noise at linear triplets of stations. *Geophysical Journal International*, *203*(2), 1149–1163. https://doi.org/10.1093/gji/ggv357

Longuet-Higgins, M. S. (1950). A theory of the origin of microseisms. *Philosophical Transactions of the Royal Society A - Mathematical Physical and Engineering Sciences*, *243*(857), 1–35. https://doi.org/10.1098/rsta.1950.0012

Ma, Y., & Clayton, R. W. (2014). The crust and uppermost mantle structure of southern Peru from ambient noise and earthquake surface wave analysis. *Earth and Planetary Science Letters*, *395*, 61–70. https://doi.org/10.1016/j.epsl.2014.03.013

Menon, R., Gerstoft, P., & Hodgkiss, W. S. (2014). Journal of geophysical research: Solid Earth on the apparent attenuation in the spatial coherence estimated from seismic arrays. *Journal of Geophysical Research: Solid Earth*, *119*, 3115–3132. https://doi.org/10.1002/2013JB010835

Mitchell, B. J. (1995). Anelastic structure and evolution of the continental crust and upper mantle from seismic surface wave attenuation. *Reviews of Geophysics*, *33*(4), 441–462. https://doi.org/10.1029/95RG02074

Mitchell, B. J., Leite, L. W. B., Yu, Y. K., & Herrmann, R. B. (1976). Attenuation of Love and Rayleigh waves across the Pacific at periods between 15 and 110 seconds. *Bulletin of the Seismological Society of America*, *66*(4), 1189–1202.

Mooney, W. D., & Kaban, M. K. (2010). The North American upper mantle: Density, composition, and evolution. *Journal of Geophysical Research*, *115*, B12424. https://doi.org/10.1029/2010JB000866

Porritt, R. W., Allen, R. M., & Pollitz, F. F. (2014). Seismic imaging east of the Rocky Mountains with USArray. *Earth and Planetary Science Letters*, *402*(C), 16–25. https://doi.org/10.1016/j.epsl.2013.10.034

Priestley, K., & McKenzie, D. (2006). The thermal structure of the lithosphere from shear wave velocities. *Earth and Planetary Science Letters*, *244*, 285–301. https://doi.org/10.1016/j.epsl.2006.01.008

Prieto, G. A., Denolle, M., Lawrence, J. F., & Beroza, G. C. (2011). On amplitude information carried by the ambient seismic field. *Comptes Rendus Geosciences*, *343*, 600–614. https://doi.org/10.1016/j.crte.2011.03.006

Prieto, G. a., Lawrence, J. F., & Beroza, G. C. (2009). Anelastic Earth structure from the coherency of the ambient seismic field. *Journal of Geophysical Research*, *114*, B07303. https://doi.org/10.1029/2008JB006067

Schmandt, B., & Lin, F. (2014). *P* and *S* wave tomography of the mantle beneath the United States. *Geophysical Research Letters*, *41*, 6342–6349. https://doi.org/10.1002/2014GL061231

Schmandt, B., Lin, F. C., & Karlstrom, K. E. (2015). Distinct crustal isostasy trends east and west of the Rocky Mountain front. *Geophysical Research Letters*, *42*, 10,290–10,298. https://doi.org/10.1002/2015GL066593

Seats, K. J., & Lawrence, J. F. (2014). The seismic structure beneath the Yellowstone volcano field from ambient seismic noise. *Geophysical Research Letters*, *41*, 8277–8282. https://doi.org/10.1002/2014GL061913

Shen, W., Ritzwoller, M. H., & Schulte-Pelkum, V. (2013). A 3-D model of the crust and uppermost mantle beneath the central and western US by joint inversion of receiver functions and surface wave dispersion. *Journal of Geophysical Research: Solid Earth*, *118*, 262–276. https://doi.org/10.1029/2012JB009602

Snieder, R. (2004). Extracting the Green's function from the correlation of coda waves: A derivation based on stationary phase. *Physical Review E*, *69*, 46610. https://doi.org/10.1103/PhysRevE.69.046610

Tromp, J., & Dahlen, F. A. (1992). Variational principles for surface wave propagation on a laterally heterogeneous Earth—II. Frequency-domain JWKB theory. *Geophysical Journal International*, *109*(3), 599–619. https://doi.org/10.1111/j.1365-246X.1992.tb00120.x

Tsai, V. C. (2010). The relationship between noise correlation and the Green's function in the presence of degeneracy and the absence of equipartition. *Geophysical Journal International*, *182*, 1509–1514. https://doi.org/10.1111/j.1365-246X.2010.04693.x

Tsai, V. C. (2011). Understanding the amplitudes of noise correlation measurements. *Journal of Geophysical Research*, *116*, B09311. https://doi.org/10.1029/2011JB008483

Tsai, V. C., Bowden, D. C., & Kanamori, H. (2017). Explaining extreme ground motion in Osaka basin during the 2011 Tohoku earthquake. *Geophysical Research Letters*, *44*, 7239–7244. https://doi.org/10.1002/2017GL074120

Viens, L., Denolle, M., Miyake, H., Sakai, S., & Nakagawa, S. (2017). Retrieving impulse response function amplitudes from the ambient seismic field. *Geophysical Journal International*, *210*(1), 210–222. https://doi.org/10.1093/gji/ggx155

Viens, L., Koketsu, K., Miyake, H., Sakai, S., & Nakagawa, S. (2016). Basin-scale Green's functions from the ambient seismic field recorded by MeSO-net stations. *Journal of Geophysical Research: Solid Earth*, *121*, 2507–2520. https://doi.org/10.1002/2016JB012796

Weaver, R. L. (2011a). On the amplitudes of correlations and the inference of attenuations, specific intensities and site factors from ambient noise. *Comptes Rendus Geosciences*, *343*, 615–622. https://doi.org/10.1016/j.crte.2011.07.001

Weaver, R. L. (2011b). On the retrieval of attenuation from the azimuthally averaged coherency of a diffuse field. *Comptes Rendus Geosciences*, *343*, 615–622. https://doi.org/10.1016/j.crte.2011.07.001

Wessel, P., Smith, W. H. F., Scharroo, R., Luis, J., & Wobbe, F. (2013). Generic mapping tools: Improved version released. *Eos, Transactions of the American Geophysical Union*, *94*(45), 409–410. https://doi.org/10.1002/2013EO450001

Yang, Y., & Forsyth, D. W. (2008). Attenuation in the upper mantle beneath Southern California: Physical state of the lithosphere and asthenosphere. *Journal of Geophysical Research*, *113*, B03308. https://doi.org/10.1029/2007JB005118